Editors' Suggestion

Flow-network-controlled shape transformation of a thin membrane through differential fluid storage and surface expansion

Yongtian Luo,[1,*] Che-Ling Ho,[2] Brent R. Helliker,[2] and Eleni Katifori[1,†]
[1]*Department of Physics and Astronomy, University of Pennsylvania, Philadelphia, Pennsylvania 19104, USA*
[2]*Department of Biology, University of Pennsylvania, Philadelphia, Pennsylvania 19104, USA*

(Received 9 September 2022; accepted 3 January 2023; published 28 February 2023)

The mechanical properties of a thin, planar material, perfused by an embedded flow network, have been suggested to be potentially changeable locally and globally by fluid transport and storage, which can result in both small- and large-scale deformations such as out-of-plane buckling. In these processes, fluid absorption and storage eventually cause the material to locally swell. Different parts can hydrate and swell unevenly, prompting a differential expansion of the surface. In order to computationally study the hydraulically induced differential swelling and buckling of such a membrane, we develop a network model that describes both the membrane shape and fluid movement, coupling mechanics with hydrodynamics. We simulate the time-dependent fluid distribution in the flow network based on a spatially explicit resistor network model with local fluid-storage capacitance. The shape of the surface is modeled by a spring network produced by a tethered mesh discretization, in which local bond rest lengths are adjusted instantaneously according to associated local fluid content in the capacitors in a quasistatic way. We investigate the effects of various designs of the flow network, including overall hydraulic traits (resistance and capacitance) and hierarchical architecture (arrangement of major and minor veins), on the specific dynamics of membrane shape transformation. To quantify these effects, we explore the correlation between local Gaussian curvature and relative stored fluid content in each hierarchy by using linear regression, which reveals that stronger correlations could be induced by less densely connected major veins. This flow-controlled mechanism of shape transformation was inspired by the blooming of flowers through the unfolding of petals. It can potentially offer insights for other reversible motions observed in plants induced by differential turgor and water transport through the xylem vessels, as well as engineering applications.

DOI: 10.1103/PhysRevE.107.024419

I. INTRODUCTION

Natural shape-morphing systems, which are ubiquitous in various living organisms and are of great interest for soft matter and biological physics, have been extensively studied by both theorists and experimentalists in attempts to understand and reproduce their dynamic morphological properties in biomimetic materials. Shape-morphing phenomena which depend on the hydraulics and mechanics of liquid flowing through living matter are widespread in animals, plants, and fungi, accommodating diverse needs for speeds and length scales of motions. The ability to absorb or release fluids in the system and the resulting variations of cell hydrostatic pressure (turgor) play a critical role in most common mechanisms for the generation and control of these shape transformations. For instance, in many invertebrate animals, from nematodes (without blood vessels) to mollusks (with blood vasculature), hydrostatic skeletons have evolved and are used to harness turgor pressure, maintain structural rigidity, and regulate body movements [1]. Likewise, plants utilize turgor pressure to generate and control both irreversible (such as growth) and reversible motion and deformation in a wide range of time scales by employing several distinct mechanisms [2,3]. For example, the Venus flytrap achieves a swift snapping closure by a mechanical instability involving hydrostatic accumulation. This is in stark contrast with other slow, gradual movements driven purely by water transport whose speed is limited by diffusion [4,5]. The latter hydraulically driven transformations include the folding and shrinking of pollen grains which dehydrate in a dry environment [6,7], and the swelling and expansion of thin and nearly flat plant structures like leaves and flower petals, which can be facilitated by fluid flow networks to overcome the spatiotemporal limitations of water diffusion on transport efficiency [8].

Examples of such flow-controlled deformations of thin sheets are manifested in the motion of petal expansion in reversible flower blooming, which is a biologically important phenomenon where petals open and close repeatedly in a 24-hour cycle. [An illustration of flower blooming is shown in Fig. 1(a).] Reversible flower opening is thought to have evolved to take place when plants need to attract insect pollinators that are only present during a specific time window in a day (e.g., during the night) [9,10]. In general, large-scale petal deformations often take place during the flowering process (reversible or irreversible), with time scales ranging between minutes and days. They frequently result from differential

*Present address: Department of Physics and Astronomy, Johns Hopkins University, Baltimore, Maryland 21218, USA; yluo58@jhu.edu
†katifori@sas.upenn.edu

FIG. 1. Biological inspiration of flow-controlled shape transformation. In each panel, the changes proceed from left to right. (a) Flower blooming of Easter lily (*Lilium longiflorum*). Snapshots taken by a Canon EOS 1200D camera. (b) The flow of fluorescence dye in the xylem venation of plantain lily (*Hosta* sp.) petals in a flower that has already bloomed, opened for visualization. Images captured by a Nikon D3300 camera. See the Appendix for the experimental approach to create these fluorescent images. (c) Cartoon illustration of the effect of a flow network on petal deformation. As incoming liquid flux (yellow) fills up empty vessels (black), the originally flat surface (1) expands differentially and buckles out of the plane (2), and eventually resumes a flatter shape as a uniform saturation of the surface is being approached (3).

tissue growth and cell elongation in the organ, which requires the regulation of water flow and turgor pressure [11]. In a hydration process, cells of different petal segments absorb water and become saturated at different rates, and swell under turgor unequally as a result of the uneven distribution of instant local water content, causing a differential expansion of petal surface which may go through remarkable buckling and shape morphing. The hydraulic behaviors of petals can partially depend on the embedded vascular networks for fluid delivery [illustrated in Fig. 1(b)] and are in many ways similar to leaf hydraulics with the same driving force of water potential [12]. Petal venation systems consist of both phloem and xylem vessels which can form a rich diversity of network architectures including various hierarchies, though usually accompanied by far lower density of stomata and much less transpiration on the surface than leaves [13,14]. Petals have also been found to make use of large hydraulic resistance (reduced conductance) and capacitance (for water storage) to sustain floral water status and turgor pressure, strengthening flower structural rigidity in a similar fashion to animal hydrostatic skeletons [15,16]. The considerations of the presence of fluid transport vasculature, the absence of noticeable water loss through evaporation, and the existence of fluid-storage capacitance are all crucial for identifying the specific dynamics of turgor change and subsequent petal motion and deformation. The biological inspiration for this work is summarized in Fig. 1, in which the cartoon in Fig. 1(c) depicts the effect of liquid movement through a flow network on the surface expansion and shape morphing (buckling) of a single petal.

In this work, we focus on the role that flow networks with a local fluid-storage function play in controlling shape transformations of thin sheets actuated by fluid flows. We are particularly interested in differential surface expansion as inspired by flower petals, and implement a simplistic theoretical model that couples hydraulic networks to deformation mechanics. Specifically, the model numerically simulates a variety of time-dependent swelling and deformation pathways, controlled by multiple uniform or hierarchical designs of flow network architecture and influenced by hydraulic traits. This way we quantitatively explore the extent to which the venation structure can affect the emergence of deformed shapes and guide these pathways, while ignoring any transpiration. Mechanical inhomogeneities in the tissue (in particular multiple layers that swell differentially), spatiotemporal variations of fluid storage ability, details of liquid transport mechanism, and biochemical regulating factors in real-life petals [10,11] are all beyond the scope of our minimal physical model.

Conventionally, studies of petal differential expansion have concentrated on the growth of certain parts of a petal, like the inner layer, midrib, edge [17], or epidermal cells versus underlying layers [18]. Motivated by these findings, engineers have created flowerlike biomimetic thin materials that exhibit large-scale deformations by incorporating anisotropic growth moduli in the plates [19,20]. The mechanical coupling between hydraulics and elasticity can play a role in deforming such a thin film with a flower shape through capillary forces [21]. We aim to draw attention to an alternative mechanism that can actuate large-scale deformations, i.e., fluid flows through venation networks, which can substantially alter the differential stored fluid distribution and subsequent surface expansion patterns. We present our modeling methods and results in Secs. II and III, respectively, in which the hierarchical network designs are inspired by leaf venation models with either branching or reticulate (loopy) structure [22,23], as petal venation is visually similar to the variety of hydraulic hierarchies contained in both monocotyledonous and dicotyledonous leaves (see micrographs in Refs. [14,24].) In Sec. IV, we discuss our results and their implications for both plant biology and biomimetics.

II. SIMULATION METHODS FOR THE COUPLED FLOW AND SPRING NETWORK MODEL

The hydrodynamic-mechanical coupling model, which we develop to simulate the spatiotemporal dynamics of fluid transport and storage (using a flow network) and to study the time-dependent resulting shape change (using a mechanical network), is elaborated in Fig. 2. The two network systems comprising the model, though essentially different in their physical properties and functions, have identical topology and connections, overlapping in real space with one-to-one correspondence between their edges and nodes. The flow network operates independently from the mechanical one, and changes

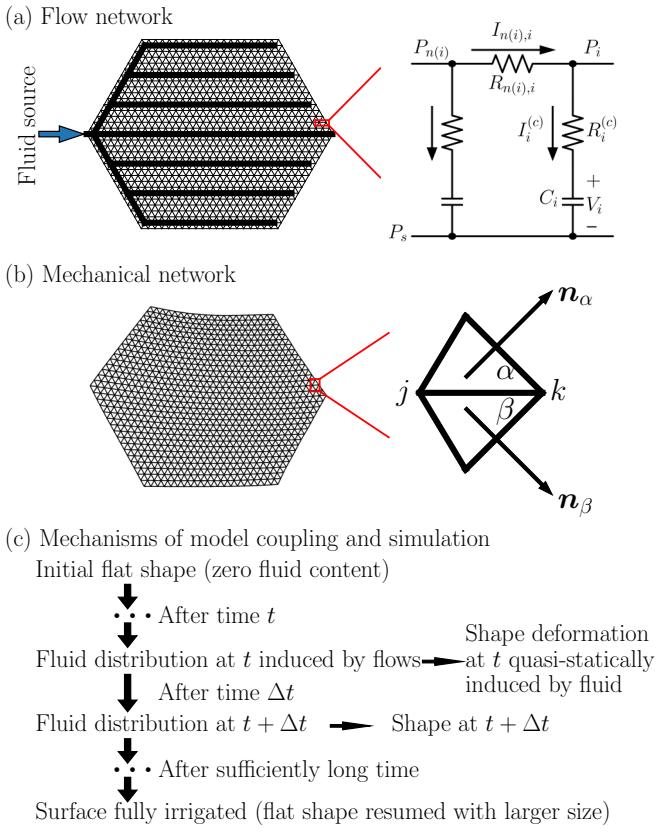

FIG. 2. The hydrodynamic-mechanical coupling model, consisting of (a) a fluid-storing flow network and (b) an overlapping mechanical network, which models the shape changes. In (a), the same hierarchy composed of major (thicker) and minor veins is used to induce the shapes in Fig. 4(b). The specific hydraulic connectivity for the resistors and capacitors is shown between a node i and one of its neighbors $n(i)$. Note that the vein segment highlighted with a red box in the network of (a) is in fact the wire linking pressures P_i and $P_{n(i)}$ through a resistor $R_{n(i),i}$, while the underlying circuit for baseline pressure P_s is not included in the diagram of the large network. At node i, C_i is the local capacitor with voltage V_i and associated resistor $R_i^{(c)}$. In (b), examples of nodes (j and k), bonds, and faces (α and β), as well as their normals ($\boldsymbol{n}_\alpha$ and $\boldsymbol{n}_\beta$) are shown. The positions of j and k in the mechanical network are the same as $n(i)$ and i in the flow network, respectively. (c) Specific coupling methods and simulation procedures.

in stored fluid are assumed to instantly affect the properties of the mechanical network and induce a deformation as detailed in Fig. 2(c). While the state of the flow network affects the state of the mechanical one, to first-order approximation we assume that their relationship is unidirectional, i.e., that the flow network is not affected by the deformation of the mechanical one. In this section we describe in detail the properties and function of each network, and specify the coupling and interactions between the flow and mechanical networks.

A. Numerical simulation of the flow network

We numerically simulate the dynamics of the flow network by making use of a spatially explicit capacitive model that we developed previously for modeling leaf hydraulics with water-storage functions [25]. This model was based on the analogy between electrical circuit and laminar flow networks [26]. Figure 2(a) illustrates an example of such a network model consisting of a venation system in which fluids flow (such as xylem vessels), where major veins with smaller resistivity (and larger conductivity) than the rest of the network are represented by thicker lines. [The simulation results of the same network can be found in Fig. 4(b).] Electric (ohmic) analogs of hydraulic traits, which include both abilities to allow fluid flow (measured by conductance or resistance) and to store fluid (measured by capacitance), are also shown for a vein segment (representative of every vein segment) between a node with index i and one of its neighbors with index $n(i)$. The driving force of the fluid flow, pressures P_i and $P_{n(i)}$ which are analogous to electric potentials, are labeled at the respective nodes. The direction of the flow current $I_{n(i),i}$ between them, analogous to electric current, is assumed to point from node $n(i)$ to i over a hydraulic resistance $R_{n(i),i}$ defined on the vein segment. Therefore, we have

$$I_{n(i),i} = \frac{P_{n(i)} - P_i}{R_{n(i),i}}. \tag{1}$$

In a hierarchical network like the one in the figure, major veins are characterized by smaller hydraulic resistance than minor veins. To model the function of fluid storage (reservoir) at each node, we define a baseline pressure P_s which is uniform throughout all the nodes. In a water-storing plant leaf or petal, the pressure P_i at a node corresponds to xylem water potential and P_s is controlled by a baseline osmotic potential. This baseline potential is determined by the most negative osmotic potential of reservoir cells (which contain aqueous solutes) when the cells hold a minimum water amount and can still behave like linear capacitors [25,27,28]. In the electric analog, a current $I_i^{(c)}$ fills the storage capacitor C_i with voltage drop V_i across its terminals (whose physical meaning in a leaf or petal is the hydrostatic pressure or turgor of storage cells) with polarity shown in Fig. 2(a) by the plus and minus signs, through a hydraulic resistance $R_i^{(c)}$. Here we have

$$I_i^{(c)} = \frac{\partial}{\partial t}\left[C_i\left(P_i - P_s - R_i^{(c)} I_i^{(c)}\right)\right] = C_i \frac{\partial P_i}{\partial t} - C_i R_i^{(c)} \frac{\partial I_i^{(c)}}{\partial t}, \tag{2}$$

as all hydraulic traits, as well as P_s, are time independent. The capacitor is shown in the process of being charged, increasing in fluid content which can be calculated readily as $W_i = C_i V_i$ anytime throughout the process. Unlike a plant leaf, the material we consider here does not contain distributed fluid sinks, i.e., surface pores (such as stomata) through which the fluid can evaporate and transpire into the atmosphere. Therefore, all fluids entering the network will eventually be absorbed and stored in capacitors when the system approaches a steady state, in which the surface is fully hydrated and pressure P_i of all the nodes is uniform and equal to the pressure of the fluid source.

Our simulation methods follow to a large degree the methods described in Ref. [25], adapted to the modeling in this work as follows. We denote $n(i)$ to be the label of any neighboring node of i, and then from mass conservation we

have

$$\sum_{n(i)} I_{n(i),i} = I_i^{(c)}. \tag{3}$$

Substituting Eqs. (1) and (2) into Eq. (3), we derive the following equation:

$$\left(\sum_{n(i)} \frac{1}{R_{n(i),i}} + \frac{1}{R_i^{(c)}}\right)\frac{\partial P_i}{\partial t} - \sum_{n(i)} \frac{1}{R_{n(i),i}}\frac{\partial P_{n(i)}}{\partial t} = \frac{1}{C_i R_i^{(c)}} \sum_{n(i)} \frac{P_{n(i)} - P_i}{R_{n(i),i}}. \tag{4}$$

The set of equations for all nodes $i = 1, 2, \ldots, N$, where N is the total number of nodes, is further organized into a matrix equation $\boldsymbol{Ax} = \boldsymbol{b}$, where the vector to be solved is

$$\boldsymbol{x} = \left(\frac{\partial P_1}{\partial t}, \frac{\partial P_2}{\partial t}, \ldots, \frac{\partial P_i}{\partial t}, \ldots, \frac{\partial P_N}{\partial t}\right)^{\mathrm{T}} \tag{5}$$

with T indicating the transpose. At time t, the ith element of vector $\boldsymbol{b}$ is

$$\boldsymbol{b}_i = \frac{1}{C_i R_i^{(c)}} \sum_{n(i)} \frac{P_{n(i)}(t) - P_i(t)}{R_{n(i),i}} \tag{6}$$

and the elements in the invertible and symmetric matrix $\boldsymbol{A}$ are

$$\boldsymbol{A}_{i,j} = \begin{cases} \sum_{n(i)} 1/R_{n(i),i} + 1/R_i^{(c)}, & i = j \\ -1/R_{j,i}, & j \text{ is neighbor of } i \\ 0, & i \neq j \text{ and } j \text{ is not neighbor of } i. \end{cases} \tag{7}$$

For a node i connected to a fluid source pressure P_p, we have $\boldsymbol{b}_i = 1/(C_i R_i^{(c)})[(P_p - P_i)/R_{p,i} + \sum_{n(i)}(P_{n(i)} - P_i)/R_{n(i),i}]$ and $\boldsymbol{A}_{i,i} = 1/R_{p,i} + \sum_{n(i)} 1/R_{n(i),i} + 1/R_i^{(c)}$, where $R_{p,i}$ is the resistance between i and the external node of fluid source.

We start the numerical simulation from an initial state $P_i(t = 0) = 0$ for the whole network. We define the baseline pressure $P_s = 0$, and thus have fluid content $W_i(t = 0) = 0$ for all the nodes. A constant positive source pressure P_p is connected to a node (here the leftmost node of the midline) at $t = 0$ to initiate the dynamic changes of P_i and W_i. At each simulation time t, we calculate $\boldsymbol{b}$ and then $\boldsymbol{x} = \boldsymbol{A}^{-1}\boldsymbol{b}$, and then update the pressures after a small time step Δt:

$$P_i(t + \Delta t) = P_i(t) + \frac{\partial P_i}{\partial t}\Delta t. \tag{8}$$

Based on $V_i = P_i - P_s - I_i^{(c)} R_i^{(c)}$, the fluid content $W_i(t)$ at node i is calculated from the instant value of $P_i(t)$:

$$W_i(t) = C_i\left(P_i(t) - P_s - R_i^{(c)} \sum_{n(i)} \frac{P_{n(i)}(t) - P_i(t)}{R_{n(i),i}}\right). \tag{9}$$

The simulation proceeds indefinitely toward all $P_i = P_p$ and $W_i^{(\max)} = C_i(P_p - P_s)$ which is the maximum fluid content. Theoretically, the process can take an exponentially long time. The average of $W_i(t)$ can be fitted to a function $a - B\exp(-t/\tau)$ where $a, B, \tau > 0$. The time constant τ is dependent on hydraulic traits, with a unit determined by the product of capacitance and resistance (see discussions in Sec. II C). The relative fluid content, $W_i(t)/W_i^{(\max)}$, is used in this work to represent the time-varying fluid content distribution in the network.

B. Numerical simulation of the mechanical network and evaluation of the three-dimensional shape

The simulation methods of the mechanical network, which captures the deformation process (differential expansion) of the simulated surface in three dimensions, are based on a tethered mesh surface discretization model (similar to a spring system) developed for the modeling of deformable membranes and spherical shells [6,7,29]. Figure 2(b) illustrates a slightly deformed mechanical network, whose buckling is induced by the hierarchy of the flow network in Fig. 2(a) that is overlaid upon it. [Other obtained shapes can be found in the simulation results of Fig. 4(b).] Also shown are the details of two neighboring faces and their edges and vertices (nodes) in this triangular tessellation of the thin membrane. Each edge behaves like a Hookean spring, and the rest length of the bond between nodes j and k [whose positions are $\boldsymbol{r}_j$ and $\boldsymbol{r}_k$ in three-dimensional (3D) space] is ρ_{jk}. The elastic stretching energy of the bond is thus

$$E_{jk}^{(\mathrm{str})} = \tfrac{1}{2}\epsilon_{jk}(|\boldsymbol{r}_j - \boldsymbol{r}_k| - \rho_{jk})^2, \tag{10}$$

where ϵ_{jk} is the discretized stretching modulus (spring constant). The elastic surface bending energy, on the other hand, is determined by the angle $\theta_{\alpha\beta}$ made by the normals of neighboring faces α and β and is calculated from their respective unit normal vectors $\boldsymbol{n}_\alpha$ and $\boldsymbol{n}_\beta$ as

$$E_{\alpha\beta}^{(\mathrm{bend})} = \kappa_{\alpha\beta}\left(1 - \cos\left(\theta_{\alpha\beta} - \theta_{\alpha\beta}^0\right)\right) = \kappa_{\alpha\beta}(1 - \boldsymbol{n}_\alpha \cdot \boldsymbol{n}_\beta), \tag{11}$$

where $\kappa_{\alpha\beta}$ is the discretized bending modulus [30,31] and the equilibrium angle is $\theta_{\alpha\beta}^0 = 0$. The total elastic energy of the mechanical network, which is the sum of stretching and bending energies of each bond and between each pair of faces, respectively, is defined as

$$E = \sum_{\langle jk\rangle} E_{jk}^{(\mathrm{str})} + \sum_{\langle\alpha\beta\rangle} E_{\alpha\beta}^{(\mathrm{bend})} = \frac{1}{2}\sum_{\langle jk\rangle} \epsilon_{jk}(|\boldsymbol{r}_j - \boldsymbol{r}_k| - \rho_{jk})^2 + \sum_{\langle\alpha\beta\rangle} \kappa_{\alpha\beta}(1 - \boldsymbol{n}_\alpha \cdot \boldsymbol{n}_\beta), \tag{12}$$

where the summations are over adjacent nodes and faces.

At simulation time $t = 0$, the initial surface shape has all bonds relaxed at their rest lengths, which are ρ_{jk}^0 at $t = 0$. As the simulation proceeds, the rest lengths ρ_{jk} enlarge with time according to the associated fluid contents at the two ending nodes of bonds [e.g., $W_j(t)$ and $W_k(t)$]. We apply a linear relationship between ρ_{jk} and the average of relative fluid contents at nodes j and k, and have

$$\rho_{jk}(t) = \rho_{jk}^0 + \frac{m_{jk}}{2}\left(\frac{W_j(t)}{W_j^{(\max)}} + \frac{W_k(t)}{W_k^{(\max)}}\right), \tag{13}$$

where $m_{jk} > 0$ so that the surface expands locally as fluid accumulates. Given the fluid content distribution generated from the flow network at time t, the total elastic energy E in Eq. (12) is provided with a particular distribution of $\rho_{jk}(t)$,

leading to a change of the shape of the mechanical network which presumably adjusts according to the new rest lengths at time scales much faster than the ones governing the fluid flow. The positions of nodes are adjusted in a quasistatic way in order to minimize E, and the system is assumed to have reached mechanical equilibrium before the next fluid flow simulation step at $t + \Delta t$. Note that the shape change is assumed to have no effect on the properties of the flow network. This unidirectional influence is summarized in Fig. 2(c).

C. Specifics of network design and architecture

In this study, we use the same regular triangular lattice for both fluid channels (flow network; see also Ref. [22]) and surface mesh discretization (mechanical network). The boundary of the network system has a hexagonal shape which is symmetric about its midline (the horizontal long axis at the center in Fig. 2) but nonequilateral. The total number of nodes is 949 including 37 nodes along the midline, and the number of edges is 2740. The network size is chosen so that the discretization of the mechanical network is finer when compared with its effective thickness [see the discussion below Eq. (14)], while also keeping the numerical simulations computationally efficient. We have tested that a coarser network with fewer nodes and edges generates simulation results that are qualitatively similar to our chosen discretization.

In the flow network, the same constant hydraulic capacitance $C_i = C$ and resistance to capacitor, $R_i^{(c)} = R_c$, are assigned to all the nodes, so that $W_i^{(\max)} = C(P_p - P_s) = W_{\max}$ is also a constant. Note that $R_{n(i),i}$ of each vein segment can be nonuniform. In the mechanical network, uniform, constant discretized stretching ($\epsilon_{jk} = \epsilon$) and bending moduli ($\kappa_{\alpha\beta} = \kappa$) are used throughout the whole network. The initial bond rest length $\rho_{jk}^0 = \rho_0$ is also identical for all the bonds. We choose a positive constant parameter $m_{jk} = m$ with a length dimension in Eq. (13) for the evaluation of rest length change. The surface shape is initially planar and undeformed at the beginning of a simulation, when all the bonds have the same length and triangular faces in the mesh grid are equilateral. The surface expands differentially as the bond lengths extend quasistatically according to Eq. (13) (induced by fluid irrigation and storage) in the simulation. When the surface is fully irrigated and all capacitors approximately contain the same amount of fluid, $W_{\max}$, the rest lengths of all the bonds are once again identical ($\rho_{jk} = \rho_0 + m$), and the surface resumes a planar shape with larger bond length and overall area. In this work, we select $\rho_0 = 1$, which is used as the basic length unit, as well as $m = 1$, so that the rest length increases from 1 to 2 from the beginning to the end of the simulation. We also choose $R_c = 1$ and $C = 2$ for the simulations, and the basic time unit in this work is hence $CR_c/2$.

The effective thickness h of the elastic membrane and regular triangular network can be calculated by using the relationships between discretized moduli and Young's modulus Y as well as Poisson ratio ν: $\epsilon = \sqrt{3}hY/2$ and $\kappa = h^3Y/[6\sqrt{3}(1-\nu^2)]$, where $\nu = 1/3$ for this discretization [6,32]. We thus obtain

$$h = 3\sqrt{\frac{(1-\nu^2)\kappa}{\epsilon}} = 2\sqrt{\frac{2\kappa}{\epsilon}}, \tag{14}$$

which is independent of bond lengths or network size and is only dependent on the ratio of discretized moduli. Using $\sqrt{\kappa/\epsilon} = 0.306$ (in the length unit $\rho_0 = 1$) in this modeling, we estimate the effective thickness to be $h = 0.8655$, which is thus always smaller than bond lengths and so the system is reasonably a good model for thin membranes.

In the next section we present the numerical simulation results of several shape transformations, all with the same mechanical design but different hierarchies of hydraulic resistance $R_{n(i),i}$ in the flow network. For the uniform flow network designs in Fig. 3, all $R_{n(i),i} = R$ are identical. Different R values are applied along with $R_c = 1$ and $C = 2$ to study the effect of edge resistance on the transformation dynamics for both fluid spreading and surface expansion. The hierarchical network designs in Figs. 4–6 are based on the parameters of the last uniform network, in which $R = 0.2$ is used for the assignment of $R_{n(i),i}$ in a hierarchy. We define the cost of each vein segment to be directly proportional to $1/R_{n(i),i}^{\gamma}$, where $\gamma = 0.5$ [22,33]. This can be understood in terms of a Poiseuille flow through a pipe of radius r_p, where the resistance R_p is proportional to $1/r_p^4$; when the cost of the pipe, K_p (amount of material), is proportional to its cross-section area (or r_p^2), K_p is thus also proportional to $1/R_p^{0.5}$. We keep the total cost of each hierarchy to be the same as that of the uniform network with $R = 0.2$, which means $\sum 1/\sqrt{R_{n(i),i}}$ over all the veins is conserved. In each hierarchy, a small resistance value (R_{maj}) and a large value ($R_{\min}$) are used for major and minor veins, respectively, which are changed for different designs but always have $R_{\text{maj}} = R_{\min}/1000$. Major veins are thicker in a real-life material and are highlighted with greater thickness in the diagrams. Three categories of hierarchies are designed, including "forklike" (Fig. 4, where major vein branches are mostly parallel to the midline), "leaflike" (Fig. 5, where branches extend from the midline), and loopy ones (Fig. 6, where major veins form loops).

In each simulation, the fluid always enters the network from the leftmost node on the midline, which is connected to a fluid source across a small resistance at $t = 0$. With simulation time step $\Delta t = 0.01$, at each integer time point ($t = 1, 2, \ldots$ until $t = 500$ for uniform networks and $t = 100$ for hierarchies), the instant distribution of relative fluid content is calculated (which is used to get the time constant τ). We then find the shape with minimum mechanical energy E in Eq. (12), initializing the optimization with either a planar shape (at the first time step) or a deformed shape (the optimized shape at a previous time point at subsequent time steps). To quantify the resulting shape, the Gaussian curvature at each node is estimated using an angular deficit method derived from the Gauss-Bonnet theorem [34]. We show in Figs. 3–6 the 3D visualizations of obtained shapes, which also illustrate time-dependent fluid distributions in colors, both for uniform networks (which, for our parameters, stay nearly flat) and for various hierarchical structures at certain time points. The 3D renderings are generated from the Mayavi package of the PYTHON programming language [35], and do not reflect the actual thickness or overall size of the membrane which enlarges gradually, but are plotted to display the surface deformation and buckling. Correlation analyses using linear regression are performed for the fluid distributions and Gaussian curvature arrangements of the resulting shapes of each hierarchical de-

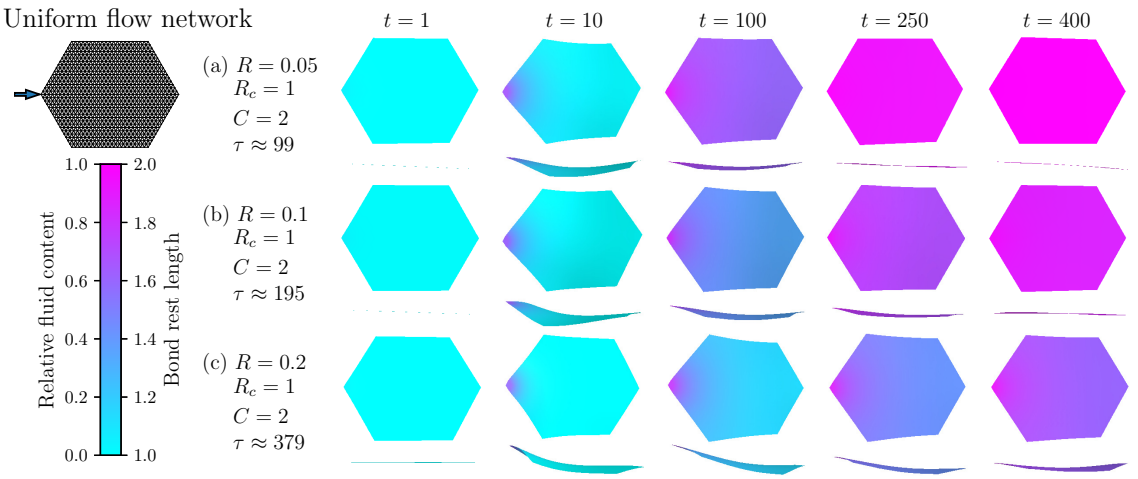

FIG. 3. Numerical simulation results of time-dependent shape transformations induced by fluid expansion in a uniform flow network. Different resistance parameters R (but identical capacitance C with associated resistance R_c) are used for (a)–(c) to generate the 3D shapes at different time t, whose side views are shown below front views to illustrate possible buckling. With larger resistance, the fluid expansion becomes slower (indicated by larger time constant τ) and the buckling lingers for a longer time.

sign from $t = 1$ to 50. Examples of the analysis performed on the loopy hierarchy are given in Fig. 7, which also includes two-dimensional (2D) plots of relative fluid distribution and Gaussian curvature whose values at each node are linearly interpolated on the surface. Summaries of linear regression results for all hierarchies, as well as more examples of such 2D plots, can be found in Figs. 8–10.

III. RESULTS

A. Uniform flow networks

For a uniform flow network embedded in a surface, such as those shown in Fig. 3, the fluid flow resembles uniform diffusion, with a speed of spreading affected by the hydraulic resistances (and capacitance). The rate of fluid spreading and the resulting shape expansion is characterized by a time constant τ estimated from the temporal changes of average fluid content over the surface. In each simulation series, the membrane keeps a relatively flat shape at the beginning, and then gradually buckles out of the plane, making a slightly curved saddle shape. The curvature of the shape first grows and then diminishes slowly with time as the fluid diffuses spatially, and ultimately, after a long period of time, the whole surface is almost uniformly hydrated and the planar shape reemerges. Apart from estimating τ from the exponential fitting of average fluid content (see Sec. II A), one can visually compare the expansion speeds of the different simulations by observing both the time- and space-dependent relative fluid content distributions, which are linearly related to local bond rest lengths and measured by the color bar, and the shape transformations represented by a front view and a side view featuring out-of-plane buckling.

In the flow network, an increase of any of the hydraulic traits R, R_c, and C will slow down the process, increase the time constant, and extend the period during which the surface buckles. This happens as a large resistance hinders the fluid movement and large capacitors require more time to fill. The effect of a large resistance R of each vein segment (edge), which increases τ almost twofold when doubled, is directly visible in Fig. 3. A selection of larger R_c or capacitance C will be accompanied by a change in the time scale of the simulations, effectively extending τ and sustaining the buckling deformations for a prolonged period. Based on the selection of large hydraulic parameters in Fig. 3(c), we design different flow network hierarchies to generate various, more pronounced shape changes of the surface.

B. Hierarchical flow networks

The hierarchical network designs, including forklike, leaflike, and loopy hierarchies, have the same hydraulic parameters used in Fig. 3(c) except for $R = 0.2$, which is used to derive the major and minor vein resistances for which the total cost of all vein segments is conserved. The high efficiency of fluid transport in major veins with much lower resistance than minor veins is apparent: in Figs. 4–6, all simulated surfaces starting with an even distribution of fluid (zero everywhere) experience an uneven irrigation process, first through major veins in a fast motion, quickly filling capacitors along these veins, and then through minor veins, gradually spreading into areas farther away in a diffusionlike manner. Correspondingly, the shape of a surface experiences large-scale deformations and buckling induced by differential expansion of the surface because of the nonuniform fluid distribution in the intermediate stages of the fluid flow simulation process. Similar to simulation results of uniform flow networks, most generated shapes in Figs. 4–6 are symmetric about the network midline, and are posted at an angle in the figures to illustrate the visual effects of buckling and deformations. After an exponentially long time, the eventually uniform distribution of fluid on the thin surface (nearly fully hydrated everywhere) produces a nearly flat configuration, similar to the starting shape. The areas proximal to fluid source (leftmost node) start to saturate with fluid and deform earlier, and also begin to flatten out earlier than areas on the distal side. The

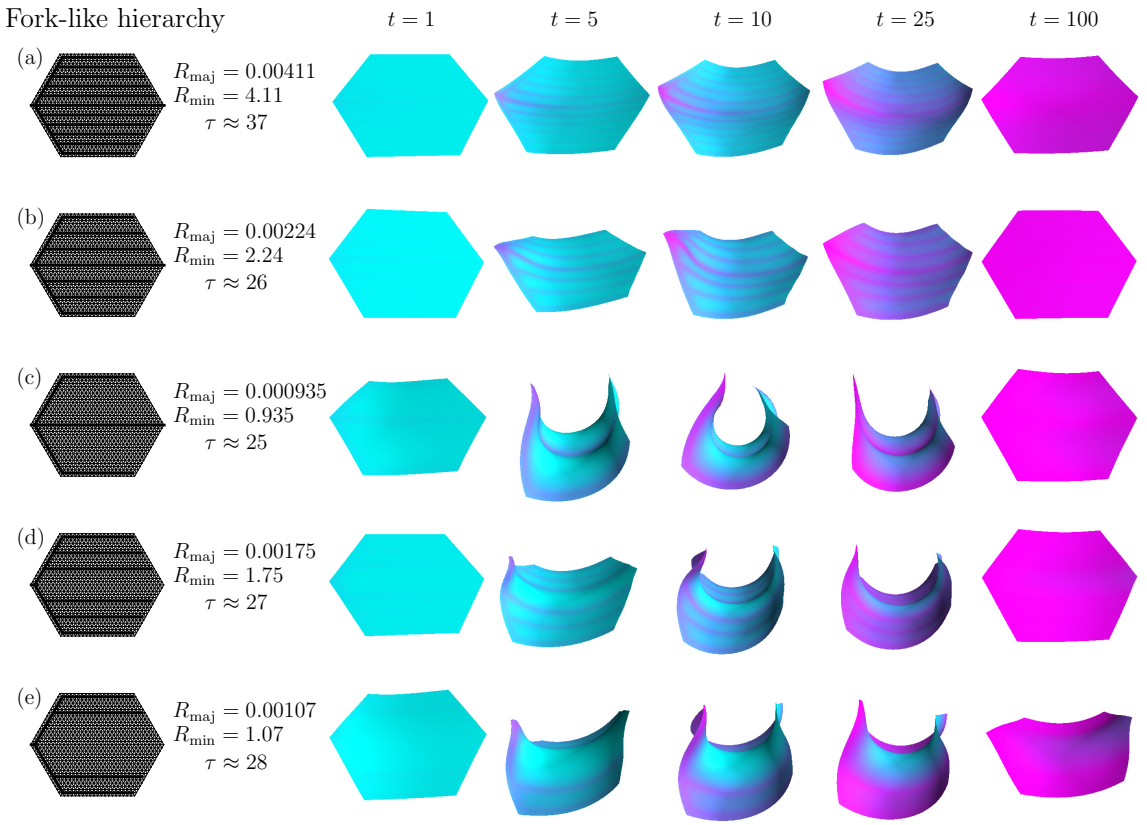

FIG. 4. Dynamic simulation results of shape transformations induced by flow networks with "forklike" hierarchies, whose hydraulic resistances of major (R_{maj}) and minor veins (R_{min}) are chosen (in addition to $R_c = 1$ and $C = 2$) so that the total cost of network is conserved. The 3D visualizations at different times t illustrate the instant fluid content distribution (whose average spreading speed is characterized by time constant τ) according to the same color bar of Fig. 3. Note that the 3D renderings, which are symmetric about their midlines, are at an angle with the paper to show the subsequent buckling from their original planes.

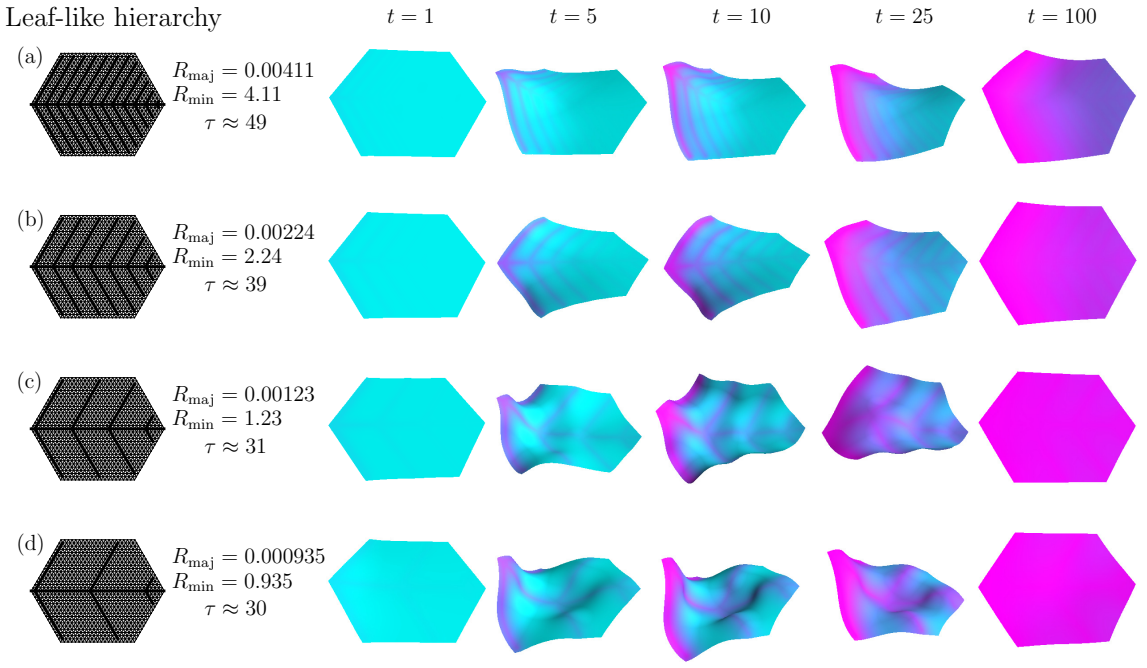

FIG. 5. Dynamic simulation results (with time t) of shape transformations induced by flow networks with "leaflike" hierarchies. See the caption of Fig. 4 for detailed information of the parameters.

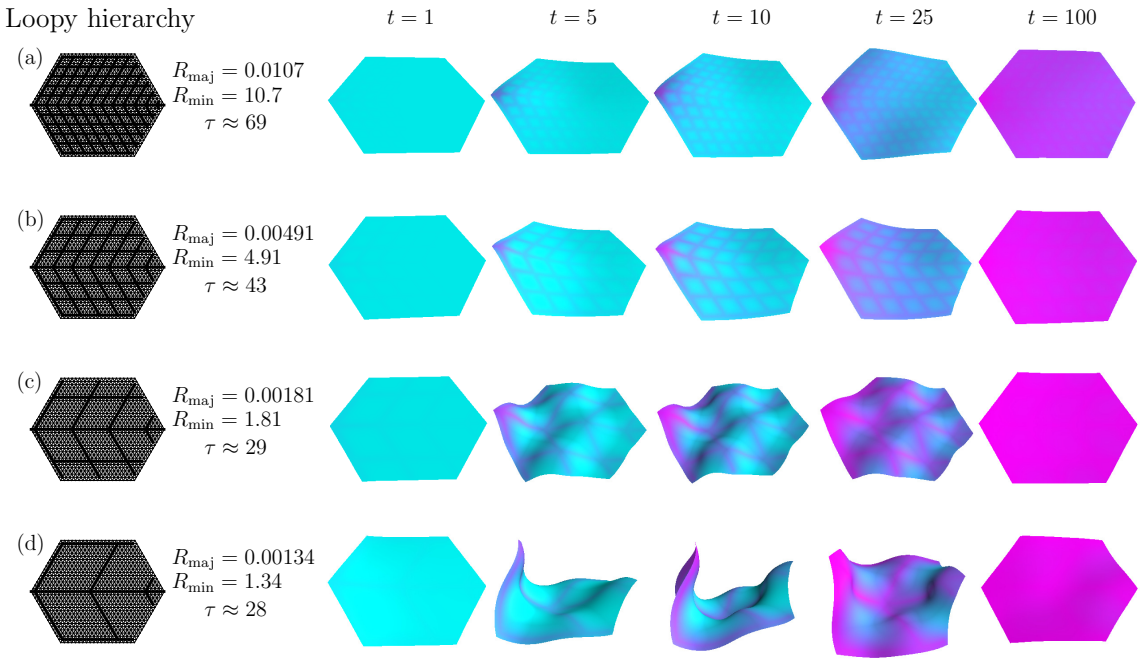

FIG. 6. Dynamic simulation results (with time t) of shape transformations induced by flow networks with loopy hierarchies. See the caption of Fig. 4 for detailed information of the parameters.

pace of hydration and length of time it takes to expand all over the surface can be characterized by the time constant τ labeled for each hierarchy.

Two relationships between structure and deformation are easily discernible among all the numerical simulation results of distinct hierarchical flow networks. First, a denser arrangement of major veins (with narrower gaps between major vein branches) leads to a smaller overall curvature change and moderately deformed shapes with less prominent buckling in our dynamic simulation process than a sparser major vein arrangement. Dense arrangements also bring about longer time constants τ, while sparse ones are generally more efficient for fluid movement over the surface on average. Second, at a particular time point, areas on the surface with relatively more fluid content tend to form concave or convex shapes sustaining a positive Gaussian curvature, whereas areas with relatively small fluid amount are more likely to form saddle shapes with a negative Gaussian curvature. These correlations increase with the extent of deformation and decline at later time stages as the fluid saturates the capacitors and the shape becomes flat, and are demonstrated with detailed calculation and analyses in Figs. 7–10. Both relationships between structure and deformation are most noticeable in the forklike hierarchy results in Fig. 4, where the dense major vein connections in Figs. 4(a) and 4(b) give rise to bowl-shaped deformations with minimal out-of-plane buckling. The magnitude of curvature variation and extent of buckling dramatically grow when major vein branches are spatially more distant from each other such as in Fig. 4(c). There the midline is formed by major veins (with higher instant fluid content) and goes through large positive curvatures before straightening out, while the areas on the two sides of the midline, which are filled with minor veins (with lower fluid content), go through saddle shapes with large negative curvatures. When the midline is formed by minor

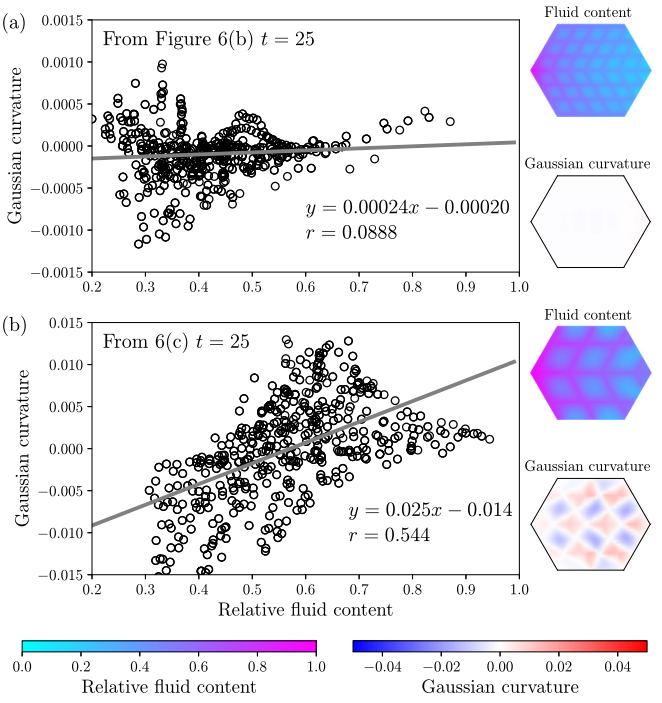

FIG. 7. Examples of correlation between local relative fluid content and Gaussian curvature over the surface obtained by linear regression at time $t = 25$, for the two loopy hierarchical designs from Figs. 6(b) and 6(c), respectively. Both the linear regression equation and correlation coefficient r are shown with each plot. (a) A small slope and low degree of correlation (small r value), and (b) a large slope and high degree of correlation. On the right-hand side of each correlation plot, the 2D plots illustrate both the instant distribution of relative fluid content and that of the estimated Gaussian curvature of the obtained shape.

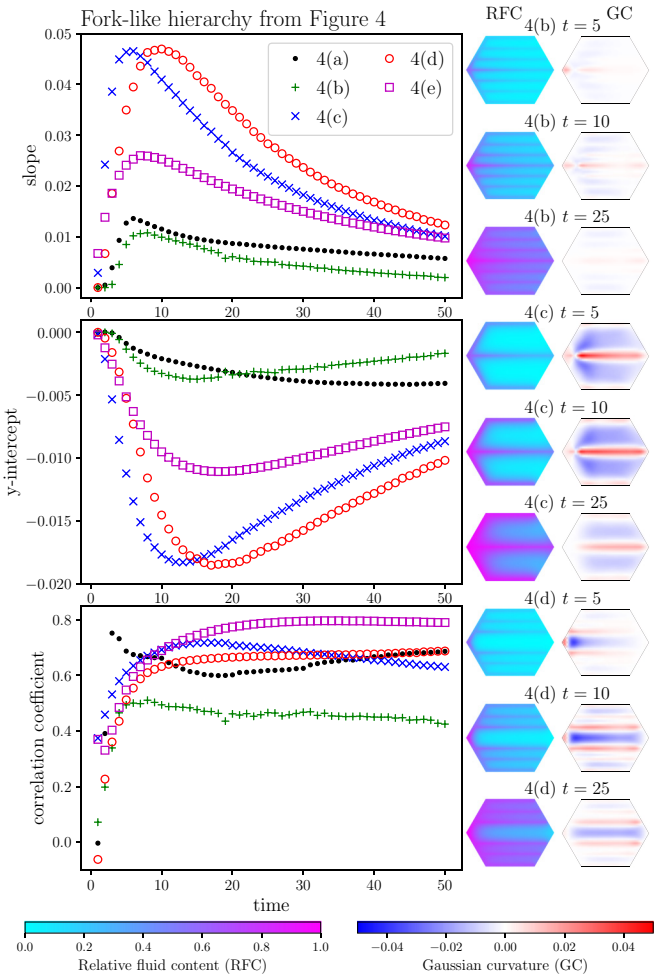

FIG. 8. The correlation between local relative fluid content and Gaussian curvature over the surface, as represented by the linear regression results (slope, y intercept, and correlation coefficient r) for each "forklike" hierarchy at each integer time point from $t = 1$ to 50. On the right side, 2D plots of fluid content (RFC) and Gaussian curvature (GC) distributions are shown for several hierarchies at certain time points (corresponding to some shapes in Fig. 4). The symbols 4(a)–4(e) represent vein patterns with the same labels as in Fig. 4.

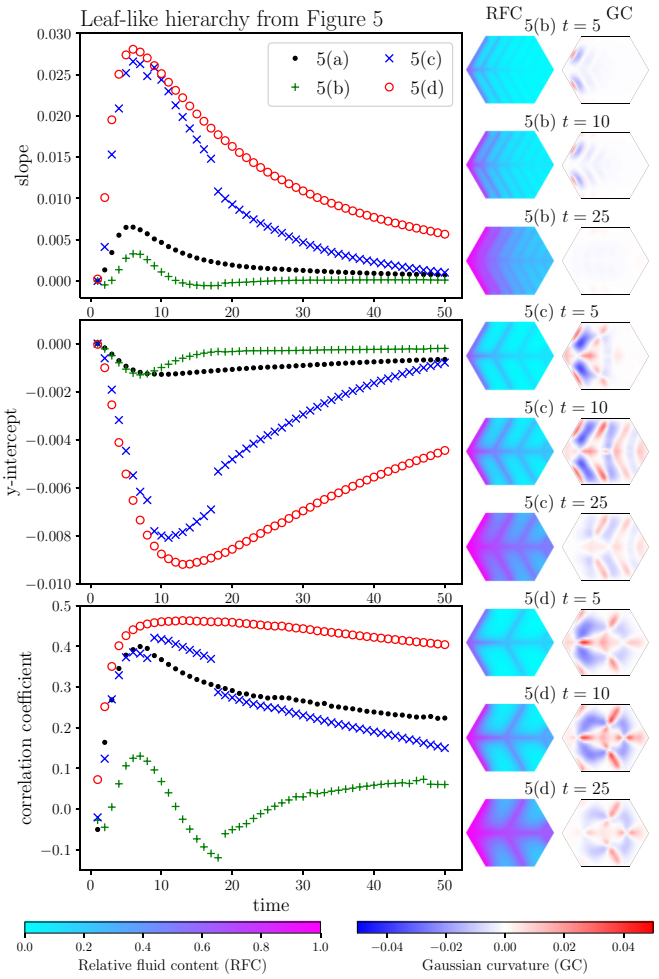

FIG. 9. Linear regression results for each "leaflike" hierarchy, with 2D plots corresponding to some shapes in Fig. 5. The symbols 5(a)–5(d) represent vein patterns with the same labels as in Fig. 5. See the caption of Fig. 8 for more information on the parameters.

veins surrounded by parallel major vein branches such as in Figs. 4(d) and 4(e) where the midline holds less fluid than its surroundings, the resulting saddle-shaped surfaces illustrate negative curvatures around the center and midline. Thus, the hierarchies drastically alter the outcome of specific shapes and curvatures according to the aforementioned observed correlations.

Similar to the forklike hierarchies, the leaflike and loopy hierarchies also generate a diverse set of dynamically changing shapes. In Fig. 5(a), showing the most dense major vein arrangement, the leaflike hierarchy leads to overall saddle shapes (unlike the bowl shapes in Fig. 4). With a smaller major vein density, shown in Fig. 5(b), the saddle shapes occur at later times (around $t = 25$) after the earlier generation of distorted, asymmetric shapes (around $t = 5$ and 10), in which the area near the fluid source is twisted at an angle with area far from the source. The transition between the twisted and saddle shapes appears to be discontinuous, and the same discontinuity also exists in the shape change between $t = 10$ and 25 in Fig. 5(c). The shape transformations in Figs. 5(c) and 5(d) show the same effects of correlations as summarized above, with more pronounced deformations.

Last, we study loopy hierarchies by adding major veins parallel to the midline onto leaflike structures, similar to superimposing the forklike and leaflike structures. With dense major veins, the formation of loops hugely reduces curvature development and suppresses large-scale buckling in Figs. 6(a) and 6(b). With smaller density (larger gaps) of major veins, the loop formation in Fig. 6(c) gives rise to fascinating shapes with alternations of concave (or convex) and saddle points on the surface (alternating positive and negative Gaussian curvatures; see Figs. 7 and 10). The loops in Fig. 6(d) appear to promote the development of curvature, bringing about more curved shapes.

C. Correlation analysis of shape and fluid distribution

The correlation between local deformation and fluid content can be quantified through linear regression of the

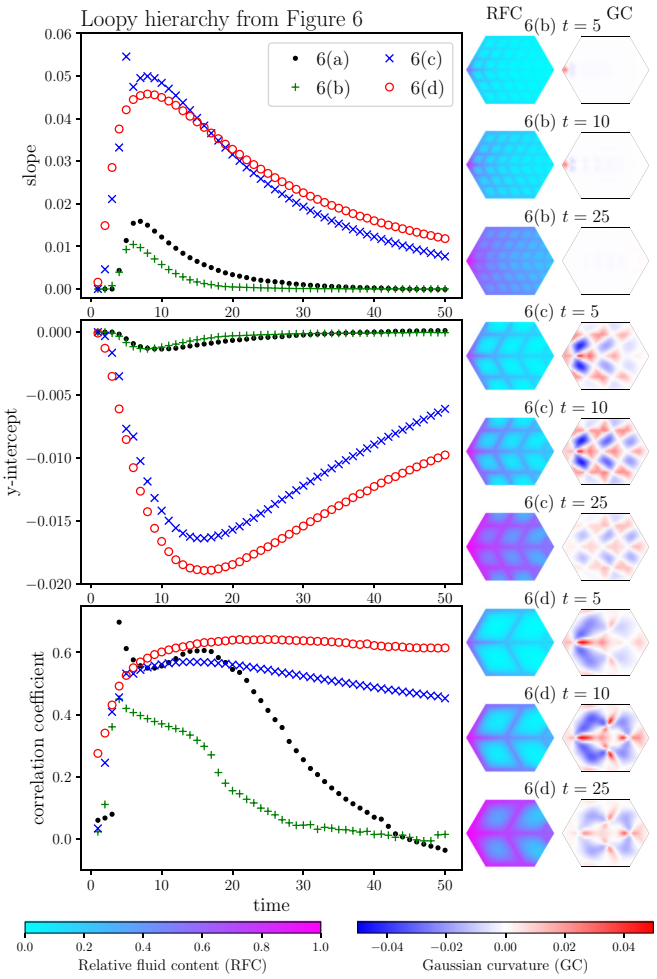

FIG. 10. Linear regression results for each loopy hierarchy, with 2D plots corresponding to some shapes in Fig. 6. The symbols 6(a)–6(d) represent vein patterns with the same labels as in Fig. 6. See the caption of Fig. 8 for more information on the parameters.

Gaussian curvature versus relative fluid content, for the optimized surface shapes in Figs. 4–6 at each simulation time point. Figure 7 specifies this type of analysis for two deformed shapes obtained at time $t = 25$ from the loopy hierarchies in Figs. 6(b) and 6(c). On the right, the instant distributions of relative fluid amount and Gaussian curvature are plotted in two-dimensional hexagons for the two loopy designs, one with minimal buckling (caused by dense major veins) and the other showing a spatial alternation of positive and negative Gaussian curvatures. In each design (except for peripheral nodes, whose curvatures are assigned zero), the Gaussian curvature at each node is then plotted against its local relative fluid content. The scatter plot including data from all these nodes is used to calculate the least squares linear fitting represented by the solid straight line, and the linear equation and correlation coefficient r. Though both correlations are positive, indicating that a more positive Gaussian curvature is more likely to emerge from higher fluid content, the architecture with dense major veins shows a weak correlation (small r) and the architecture with sparse major veins tends to maintain a strong correlation (large r). The magnitude of slope, on the other hand, serves as a measure of shape change, with large slopes indicating prominent deformation. Thus both observations mentioned above about the effects of major vein density are confirmed by this analysis.

Correlation analyses carried out by using the same method as in Fig. 7 (containing linear fit slope, y intercept, and correlation coefficient, all of which vary with time) and applied to forklike, leaflike, and loopy hierarchy results (optimized surface shapes) from time $t = 1$ to 50, are summarized in Figs. 8–10, respectively. Similar 2D hexagonal plots to those of relative fluid content and Gaussian curvature in Fig. 7 are generated for several selected shapes found in Figs. 4(b)–4(d), 5(b)–5(d), and 6(b)–6(d). They can be located on the summary plots of the linear regression results. In general, the resulting slopes are positive and y intercepts are negative, and they are approximately negatively related for a certain hierarchy: as the slope becomes more positive, the corresponding y intercept generally becomes more negative, but slightly lags behind the change of slope and reaches a minimum at a little later time than the peak of slope. The correlation coefficients (as well as both slopes and y intercepts) are generally larger in magnitude for designs with less dense major vein arrangements (wider gaps between major vein branches). These findings generalize the observations from Fig. 7 about positive correlations and their strengths (and also intensities of deformation) in different hierarchies to basically all obtained shapes at all times, with sparser major vein connections giving rise to stronger correlations (and larger deformations). The dynamic variations of linear fit results follow comparable trends with time for all hydraulic hierarchical categories. The correlation sharply increases, initially starting with empty capacitors and undeformed surface, rapidly growing as represented by the correlation coefficient along with the intensive shape transformation and curvature development (in terms of slope, with y intercept becoming more negative) that happen simultaneously. After reaching a peak correlation (which is also near the point of maximum deformation and curvature forming of the surface) it finally diminishes in a slow pace, corresponding to the gradual decline of curving and buckling to a uniformly expanded flat shape with full capacitors. In this process, the Gaussian curvature plots clearly exhibit the movement of curvature formation from the near side of the fluid source (left side of the surface) to the far side (right side) following the fluid spread and differential expansion. The discontinuous shape transitions in leaflike hierarchies of Figs. 5(b) and 5(c) are also reflected by the discontinuity in one or more of the linear regression outcomes at around $t = 18$ in Fig. 9, for example, the breaking of the correlation coefficient trend for both Figs. 9(b) and 9(c) and also the jumping of slope and y intercept for 9(c).

Further rescaling the emergent curvature patterns (e.g. with respect to the gap distance between two major veins) to explore a more general correlation between Gaussian curvature and fluid content distribution (to be applicable to all kinds of hierarchies) could be complex. The amount of generated curvature is a complicated function of the bending and stretching moduli, as well as the differential swelling, and a simple rescaling of length cannot easily capture these dependencies. Furthermore, this rescaling may work to some degree for a continuous surface, but is limited in this work by the dis-

cretized nature of our mechanical network (spring system) and its internal length scale, which is the original bond rest length of an edge (and is also the unit length we use). Since the bond lengths in the network are not negligible compared to gaps between major veins, the obtained correlations should be understood with the consideration of this size comparison. Specifically, even with the same degree of variation of relative fluid content, the curvature formation in a network with smaller major vein gaps is suppressed by the discretization to a greater extent than one with larger gaps. This difference enhances the correlation contrasts among the various hierarchical designs in Figures 8–10. An extension of these observations from networking systems to a continuous limit is out of the scope of this study.

IV. DISCUSSION

Our work contributes to the large volume of literature regarding the shape morphing of thin membranes related to hydraulics, by revealing the significant roles of fluid delivery and storage capability. We show that, besides helping to withstand drought conditions [25], the large hydraulic capacitance in petals can also contribute to the extension of petal buckling and unfolding period (see Sec. III A), affecting the time scale of opening in many species. Our work, however, was only inspired by biology, and ignores biological complexity, such as the biochemistry that might affect the storage capacity of the cells. We also simplified the coupling between hydrodynamics and mechanics in our model, by only taking into account how the fluid flow can change the surface shape but not the effects of shape transformations on flow network changes. This is acceptable in a first-order approximation in order to focus on the most fundamental physics of these phenomena. The inverse effects, which can deform the conduit cross section and lead to variations of hydraulic conductance in the flow network of a living system, can be important for physiological fluid-structure interactions in both animals [36] and plants [37,38]. To study a real-life system where the higher-order effects are not negligible, rigorous investigations should be applied to the particular material being explored to find out and implement the specific dependence of flow network properties on surface deformations, which is usually complicated and distinct from other materials. In order to investigate the extent to which our findings are relevant for real-life petals, experimentalists can apply novel, advanced measurement approaches on petals, such as time-lapse imaging and video of deformation processes [39], and also innovative techniques to extract flow network architecture [40,41] or to keep track of fluid movement using fluorescent dyes [22,42]. Ideal species to be tested are those whose flowers open and close repeatedly (e.g., opening during the night and closing during the day, or vice versa) with a pace not too fast or slow, and with a mechanism clearly due to the regulation of water loss or refill, such as the *Silene* species pointed out in Ref. [9].

The existence of hierarchies in vascular flow networks was shown to optimize transport efficiency (with branches [43]) and be robust to damages and fluctuations (with loops [44]). Similarly, in mechanical networks, the network rigidity was shown to be strengthened by hierarchical elastic structures [45]. In this work, we demonstrate another straightforward impact of the topology of venation on thin sheet mechanics, through local fluid absorption, differential expansion, and ensuing deformation. With fluid quickly spreading through low-resistance major vein highways (confirmed experimentally in leaves [46]), fluid storage elements are rapidly filled up in their vicinity undergoing local growth. Unless there exists a nonlocal feedback control mechanism, the surface cannot remain flat when growing [47].

The differential expansion due to fluid storage forces the surface to bend into a buckled shape, in which positive Gaussian curvatures build up in relatively liquid-rich areas and negative ones form in liquid-poor regions. The emergence of saddle shapes similar to those in Figs. 4 and 5 has been observed in leaves and petals and modeled using differential growth, in addition to rippling patterns near the surface margin due to edge elongation [17,48,49]. Similar patterns are produced by some of our modeling results [Figs. 5(c) and 6(c)] with an overall surface undulation (because of the spatial alternations of positive and negative Gaussian curvatures). The undulating shapes in this work, controlled by flows, can be compared to patterns emerging on confined, intrinsically curved thin shells arising from their surface area mismatch with the geometry of the confinement [50–52]. Hence, our work provides an alternative mechanism for the appearance of nontrivial deformations of a thin shell in a physical or biological system in addition to well-established methods.

These deformation mechanisms, including the one in this study, tend to emphasize the geometric aspects of shape transformations by focusing on surface growth and expansion. However, mechanical factors can be easily introduced to our model by having stretching and bending moduli in Eq. (12), rather than just bond rest length, also increase with the buildup of local fluid content. This would correspond to a differential stiffening, which may accelerate the restoration of flat shape.

Our work focuses on analyzing how the topology and hierarchy of irrigation networks affect the flow-controlled deformation dynamics of the fluid absorbing membrane. The connectivity of our model flow network was selected to represent broad classes of biologically inspired networks. All of the "forklike,""leaflike," or loopy hierarchies of major veins were readily observed in the micrographs of flower petals of several dicot species [14,16]. The branching designs resembling leaves (Fig. 5) and reticulate ones with loops (Fig. 6) are actually inspired by the model leaf venations in Ref. [23]. Some network models were developed as inspired by the leaf of a monocotyledon (like wheat [53]) or dicotyledon (like laurel [54]), in which square grids were applied and multiple levels of resistances were assigned to different degrees of veins. In this work, on the contrary, we only apply two resistance values, different by a factor of 1000, to major and minor veins to focus on the fundamental aspects of hierarchy. We also implement a triangle, rather than a square, mesh grid with hexagonal boundary which was also used for leaf models previously [22,40]. The triangular grid of the fluid flow system can be readily used for the architecture of the mechanical network that models the elastic properties and shape changes of the thin sheet surface, as triangle grid meshes capture both stretching and bending. Our simple model with only very basic components can be easily augmented to incorporate spatiotemporal inhomogeneities into the flow and mechanical

networks. For example, there can be more than two levels of vein resistance to capture the tapering and reduction of conductance in major veins from petiole (fluid source) to the margin [23]. The effect of transpiration can be added by setting internal nodes as flow sinks, and the mechanical properties can be spatiotemporally variable, reflecting the in-plane anisotropy of the thin material (e.g., the diversification of petal cell elasticity) or more complicated effects of fluid accumulation.

The numerical findings in this work, especially the local correlations between surface curvature and fluid content in the thin membrane, can also provide helpful insights into how the conformation of a swellable thin material can be fine tuned. This fine tuning is achieved by adjusting the fluid distribution. Given a target surface configuration, the arrangement of curvatures can be calculated, and then correlated to relative fluid contents through the correspondences found in Figs. 7–10. Though the shapes created in this work are dynamical and transient, one can potentially program the surface into a desirable shape with high confidence (based on a linear relationship with strong correlation) by holding the underlying local fluid contents in a steady state through an arresting mechanism. Practical, quantitative correlations will need to be determined through experiments and not directly from our numerical results based on the minimal model.

Formerly, by manipulating deforming mechanisms like differential growth, engineers have fabricated thin sheets responsive to environmental stimuli, making a large variety of structures including nematic glass cantilevers [55,56] and temperature-sensitive copolymer disks [57], which can buckle when being heated or cooled. Expansive computational studies and analytical calculations have also been carried out in order to design real physical systems that harness differential swelling to transform into intended shapes when needed [58,59]. Our work serves as a complement to this field by involving fluid flow and storage as a controlling factor behind the swelling. A similar actuation principle was recently applied to macroscopic air-filled rubber plates embedded with airway channel networks, which cause shape morphing when being inflated [60,61]. For this work, notably, hydrogel polymers, which enlarge in size when immersed in water and have been made into numerous conformations in biomimetic four-dimensional (4D) printing [19], appear to be an ideal material for the fabrication of deformable thin sheets implanted with a microfluidic channel network, which can possibly test our modeling results. Microchannels embedded in thin films have already been used to simulate plant hydraulics, with one example in silicone PDMS [62] and another in hydrogel PHEMA [63], and also embedded in liquid crystal elastomer sheets to preprogram intrinsic spontaneous curvatures [64,65]. The combination of microfluidics and micromechanics in a hydrogel-based soft membrane prone to flows can recreate the coupling effects in our network model, whose major veins are explicitly mimicked by the channels and minor veins implicitly approximated by the rest of the surface where fluids diffuse and remain, and then the dynamic deformation pathways can be scrutinized physically. Overall, our study in this work reveals a plethora of possibilities in physics, biology, and applied science for future theoretical, computational and experimental investigations to further discover.

ACKNOWLEDGMENTS

The authors acknowledge support from NSF-IOS, Award No. 1856587, and thank Shu Yang for helpful discussions.

APPENDIX: EXPERIMENTAL METHOD TO CAPTURE PETAL FLUORESCENT IMAGES IN FIGURE 1(b)

Hosta sp. was collected at the University of Pennsylvania, brought back to the laboratory, and recut under water immediately. Right before the measurement, the flower was cut, flattened, and affixed onto a black background using clear tape. At time 0, the cut end of the pedicel was submerged in a Petri dish with 0.1% fluorescein solution (fluorescein free acid, Honeywell Fluka, in 15 mM KCl solution of pH 8). The Petri dish was covered with foil paper to prevent any fluorescent noise. Images were taken in a photo light box to eliminate any light source from the laboratory. In the photo light box, the light was provided by an LED growth light strip with photosynthetic photon flux density of $\approx 300\ \mu\mathrm{mol\,m^{-2}\,s^{-1}}$. Images were taken every 120 s with a Nikon D3300 camera and a color blocking filter (Filter Orange No. 22, Heliopan, Munich) mounted on a tripod stand and connected to a PC with the digiCamControl software.

[1] R. Monahan-Earley, A. M. Dvorak, and W. C. Aird, Evolutionary origins of the blood vascular system and endothelium, J. Thromb. Haemostasis **11**, 46 (2013).

[2] J. Dumais and Y. Forterre, "Vegetable dynamicks": The role of water in plant movements, Annu. Rev. Fluid Mech. **44**, 453 (2012).

[3] Y. Forterre, Slow, fast and furious: Understanding the physics of plant movements, J. Exp. Bot. **64**, 4745 (2013).

[4] Y. Forterre, J. M. Skotheim, J. Dumais, and L. Mahadevan, How the Venus flytrap snaps, Nature (London) **433**, 421 (2005).

[5] J. M. Skotheim and L. Mahadevan, Physical limits and design principles for plant and fungal movements, Science **308**, 1308 (2005).

[6] E. Katifori, S. Alben, E. Cerda, D. R. Nelson, and J. Dumais, Foldable structures and the natural design of pollen grains, Proc. Natl. Acad. Sci. USA **107**, 7635 (2010).

[7] E. Couturier, J. Dumais, E. Cerda, and E. Katifori, Folding of an opened spherical shell, Soft Matter **9**, 8359 (2013).

[8] E. Katifori, The transport network of a leaf, C. R. Phys. **19**, 244 (2018).

[9] W. G. van Doorn and U. van Meeteren, Flower opening and closure: A review, J. Exp. Bot. **54**, 1801 (2003).

[10] W. G. van Doorn and C. Kamdee, Flower opening and closure: An update, J. Exp. Bot. **65**, 5749 (2014).

[11] L. Beauzamy, N. Nakayama, and A. Boudaoud, Flowers under pressure: Ins and outs of turgor regulation in development, Ann. Bot. **114**, 1517 (2014).

[12] L. Sack and N. M. Holbrook, Leaf hydraulics, Annu. Rev. Plant Biol. **57**, 361 (2006).

[13] A. B. Roddy, C. M. Guilliams, T. Lilittham, J. Farmer, V. Wormser, T. Pham, P. V. A. Fine, T. S. Feild, and T. E. Dawson, Uncorrelated evolution of leaf and petal venation patterns across the angiosperm phylogeny, J. Exp. Bot. **64**, 4081 (2013).

[14] F.-P. Zhang and T. J. Brodribb, Are flowers vulnerable to xylem cavitation during drought? Proc. R. Soc. London B **284**, 20162642 (2017).

[15] A. B. Roddy, C. R. Brodersen, and T. E. Dawson, Hydraulic conductance and the maintenance of water balance in flowers, Plant Cell Environ. **39**, 2123 (2016).

[16] A. B. Roddy, G.-F. Jiang, K. Cao, K. A. Simonin, and C. R. Brodersen, Hydraulic traits are more diverse in flowers than in leaves, New Phytol. **223**, 193 (2019).

[17] H. Liang and L. Mahadevan, Growth, geometry, and mechanics of a blooming lily, Proc. Natl. Acad. Sci. USA **108**, 5516 (2011).

[18] X. Huang, Y. Hai, and W.-H. Xie, Anisotropic cell growth-regulated surface micropatterns in flower petals, Theor. Appl. Mech. Lett. **7**, 169 (2017).

[19] A. S. Gladman, E. A. Matsumoto, R. G. Nuzzo, L. Mahadevan, and J. A. Lewis, Biomimetic 4D printing, Nat. Mater. **15**, 413 (2016).

[20] W. M. van Rees, E. Vouga, and L. Mahadevan, Growth patterns for shape-shifting elastic bilayers, Proc. Natl. Acad. Sci. USA **114**, 11597 (2017).

[21] B. Roman and J. Bico, Elasto-capillarity: Deforming an elastic structure with a liquid droplet, J. Phys.: Condens. Matter **22**, 493101 (2010).

[22] E. Katifori, G. J. Szöllősi, and M. O. Magnasco, Damage and Fluctuations Induce Loops in Optimal Transport Networks, Phys. Rev. Lett. **104**, 048704 (2010).

[23] A. D. McKown, H. Cochard, and L. Sack, Decoding leaf hydraulics with a spatially explicit model: Principles of venation architecture and implications for its evolution, Am. Nat. **175**, 447 (2010).

[24] L. Sack and C. Scoffoni, Leaf venation: Structure, function, development, evolution, ecology and applications in the past, present and future, New Phytol. **198**, 983 (2013).

[25] Y. Luo, C.-L. Ho, B. R. Helliker, and E. Katifori, Leaf water storage and robustness to intermittent drought: A spatially explicit capacitive model for leaf hydraulics, Front. Plant Sci. **12**, 725995 (2021).

[26] H. A. Stone, Introduction to fluid dynamics for microfluidic flows, in *CMOS Biotechnology*, edited by H. Lee, R. M. Westervelt, and D. Ham (Springer, Boston, 2007), pp. 5–30

[27] J. A. C. Smith, P. J. Schulte, and P. S. Nobel, Water flow and water storage in *Agave deserti*: Osmotic implications of crassulacean acid metabolism, Plant Cell Environ. **10**, 639 (1987).

[28] H. G. Jones, *Plants and Microclimate: A Quantitative Approach to Environmental Plant Physiology*, 3rd ed. (Cambridge University Press, Cambridge, UK, 2013).

[29] H. S. Seung and D. R. Nelson, Defects in flexible membranes with crystalline order, Phys. Rev. A **38**, 1005 (1988).

[30] Y. Kantor and D. R. Nelson, Phase transitions in flexible polymeric surfaces, Phys. Rev. A **36**, 4020 (1987).

[31] G. Gompper and D. M. Kroll, Random surface discretization and the renormalization of the bending rigidity, J. Phys. I **6**, 1305 (1996).

[32] M. Kot, H. Nagahashi, and P. Szymczak, Elastic moduli of simple mass spring models, Vis. Comput. **31**, 1339 (2015).

[33] S. Bohn and M. O. Magnasco, Structure, Scaling, and Phase Transition in the Optimal Transport Network, Phys. Rev. Lett. **98**, 088702 (2007).

[34] M.-S. Hartig, Approximation of Gaussian curvature by the angular defect: An error analysis, Math. Comput. Appl. **26**, 15 (2021).

[35] P. Ramachandran and G. Varoquaux, Mayavi: 3D visualization of scientific data, Comput. Sci. Eng. **13**, 40 (2011).

[36] M. Heil and A. L. Hazel, Fluid-structure interaction in internal physiological flows, Annu. Rev. Fluid Mech. **43**, 141 (2011).

[37] H. Cochard, F. Froux, S. Mayr, and C. Coutand, Xylem wall collapse in water-stressed pine needles, Plant Physiol. **134**, 401 (2004).

[38] P. S. Bouche, S. Delzon, B. Choat, E. Badel, T. J. Brodribb, R. Burlett, H. Cochard, K. Charra-Vaskou, B. Lavigne, S. Li, S. Mayr, H. Morris, J. M. Torres-Ruiz, V. Zufferey, and S. Jansen, Are needles of *Pinus pinaster* more vulnerable to xylem embolism than branches? New insights from X-ray computed tomography, Plant Cell Environ. **39**, 860 (2016).

[39] T. Portet, Z. R. Cohen, G. J. Goetz, N. Panek, P. N. Holmes, S. A. Stephens, T. Varga, and S. L. Keller, Ripples at edges of blooming lilies and torn plastic sheets, Biophys. J. **121**, 2389 (2022).

[40] E. Katifori and M. O. Magnasco, Quantifying loopy network architectures, PLoS One **7**, e37994 (2012).

[41] A. Vasco, M. Thadeo, M. Conover, and D. C. Daly, Preparation of samples for leaf architecture studies, a method for mounting cleared leaves, Appl. Plant Sci. **2**, 1400038 (2014).

[42] W. Liu, Y. Luo, L. Wang, T. Luo, Y. Peng, and L. Wu, Water transport in leaf vein systems and the flow velocity measurement with a new method, J. Plant Physiol. **204**, 74 (2016).

[43] H. Ronellenfitsch and E. Katifori, Global Optimization, Local Adaptation, and the Role of Growth in Distribution Networks, Phys. Rev. Lett. **117**, 138301 (2016).

[44] H. Ronellenfitsch and E. Katifori, Phenotypes of Vascular Flow Networks, Phys. Rev. Lett. **123**, 248101 (2019).

[45] H. Ronellenfitsch, Optimal Elasticity of Biological Networks, Phys. Rev. Lett. **126**, 038101 (2021).

[46] M. A. Zwieniecki, P. J. Melcher, C. K. Boyce, L. Sack, and N. M. Holbrook, Hydraulic architecture of leaf venation in *Laurus nobilis* L., Plant Cell Environ. **25**, 1445 (2002).

[47] S. Al-Mosleh and L. Mahadevan, How to grow a flat leaf, arXiv:2203.15077.

[48] H. Liang and L. Mahadevan, The shape of a long leaf, Proc. Natl. Acad. Sci. USA **106**, 22049 (2009).

[49] E. Sharon, M. Marder, and H. Swinney, Leaves, flowers and garbage bags: Making waves, Am. Sci. **92**, 254 (2004).

[50] H. Aharoni, D. V. Todorova, O. Albarrán, L. Goehring, R. D. Kamien, and E. Katifori, The smectic order of wrinkles, Nat. Commun. **8**, 15809 (2017).

[51] O. Albarrán, D. V. Todorova, E. Katifori, and L. Goehring, Curvature controlled pattern formation in floating shells, arXiv:1806.03718.

[52] I. Tobasco, Y. Timounay, D. Todorova, G. C. Leggat, J. D. Paulsen, and E. Katifori, Exact solutions for the wrinkle patterns of confined elastic shells, Nat. Phys. **18**, 1099 (2022).

[53] D. P. Altus, M. J. Canny, and D. R. Blackmann, Water pathways in wheat leaves. II: Water-conducting capacities and vessel diameters of different vein types, and the behaviour of the integrated vein network, Aust. J. Plant Physiol. **12**, 183 (1985).

[54] H. Cochard, A. Nardini, and L. Coll, Hydraulic architecture of leaf blades: Where is the main resistance? Plant Cell Environ. **27**, 1257 (2004).

[55] M. Warner, C. D. Modes, and D. Corbett, Curvature in nematic elastica responding to light and heat, Proc. R. Soc. London A **466**, 2975 (2010).

[56] M. Warner, C. D. Modes, and D. Corbett, Suppression of curvature in nematic elastica, Proc. R. Soc. London A **466**, 3561 (2010).

[57] J. Kim, J. A. Hanna, M. Byun, C. D. Santangelo, and R. C. Hayward, Designing responsive buckled surfaces by halftone gel lithography, Science **335**, 1201 (2012).

[58] M. A. Dias, J. A. Hanna, and C. D. Santangelo, Programmed buckling by controlled lateral swelling in a thin elastic sheet, Phys. Rev. E **84**, 036603 (2011).

[59] P. Nardinocchi, M. Pezzulla, and L. Teresi, Anisotropic swelling of thin gel sheets, Soft Matter **11**, 1492 (2015).

[60] E. Siéfert, E. Reyssat, J. Bico, and B. Roman, Bio-inspired pneumatic shape-morphing elastomers, Nat. Mater. **18**, 24 (2019).

[61] E. Siéfert, E. Reyssat, J. Bico, and B. Roman, Programming stiff inflatable shells from planar patterned fabrics, Soft Matter **16**, 7898 (2020).

[62] X. Noblin, L. Mahadevan, I. A. Coomaraswamy, D. A. Weitz, N. M. Holbrook, and M. A. Zwieniecki, Optimal vein density in artificial and real leaves, Proc. Natl. Acad. Sci. USA **105**, 9140 (2008).

[63] T. D. Wheeler and A. D. Stroock, The transpiration of water at negative pressures in a synthetic tree, Nature (London) **455**, 208 (2008).

[64] Y. Xia, G. Cedillo-Servin, R. D. Kamien, and S. Yang, Guided folding of nematic liquid crystal elastomer sheets into 3D via patterned 1D microchannels, Adv. Mater. **28**, 9637 (2016).

[65] H. Aharoni, Y. Xia, X. Zhang, R. D. Kamien, and S. Yang, Universal inverse design of surfaces with thin nematic elastomer sheets, Proc. Natl. Acad. Sci. USA **115**, 7206 (2018).